Evidence for Ectopic Neurotransmission at a Neuronal Synapse

One Sentence Summary: A Monte Carlo model of a ganglionic synapse reconstructed with high-resolution serial EM tomography predicts activation of nicotinic receptors by non-traditional neurotransmitter release.

Jay S. Coggan[1,3]*, Thomas M. Bartol[1,8]*, Eduardo Esquenazi[3,5], Joel R. Stiles[6,7], Stephan Lamont[3], Maryann E. Martone[3,4], Darwin K. Berg[5], Mark H. Ellisman[3,4], Terrence J. Sejnowski[1,2,5,8]

[1] Computational Neurobiology Laboratory, The Salk Institute, La Jolla, California 92037, U.S.A.

[2] Howard Hughes Medical Institute, 4000 Jones Bridge Rd. Chevy Chase, MD, 20815, U.S.A.

[3] National Center for Microscopy and Imaging Research, University of California, San Diego, La Jolla, California 92093, U.S.A.

[4] Department of Neurosciences, School of Medicine, University of California, San Diego, La Jolla, California 92093, U.S.A.

[5] Division of Biological Sciences, University of California, San Diego, La Jolla, California 92093, U.S.A.

[6] Pittsburgh Supercomputing Center, Carnegie Mellon University, Pittsburgh, Pennsylvania 15213, U.S.A.

[7] Department of Neuroscience, University of Pittsburgh, Pittsburgh, Pennsylvania 15260, U.S.A.

[8] Center for Theoretical Biological Physics, University of California, San Diego, La Jolla, California, 92093-0374.

* Co-first authors
To whom correspondence should be addressed: terry@salk.edu

Abstract

Neurotransmitter release is well known to occur at specialized synaptic regions that include presynaptic active zones and postsynaptic densities. At cholinergic synapses in the chick ciliary ganglion, however, membrane formations and physiological measurements suggest that release distant from postsynaptic densities can activate the predominantly extrasynaptic α7 nicotinic receptor subtype. We explored such ectopic neurotransmission with a novel model synapse that combines Monte Carlo simulations with high-resolution serial electron microscopic tomography. Simulated synaptic activity is consistent with experimental recordings of miniature excitatory postsynaptic currents only when ectopic transmission is included in the model, broadening the possibilities for mechanisms of neuronal communication.

Throughout the nervous system, release of synaptic vesicles from presynaptic nerve terminals is thought to be associated with pre- and postsynaptic specializations including active zones (AZs) and postsynaptic densities (PSDs). Release of neurotransmitter vesicles at extrasynaptic sites (ectopic release) has been suggested by the presence of morphologically docked vesicles distant from PSDs in electron micrographs from tissues including the ribbon synapses of bipolar neurons (*1*) and saccular hair cells (*2*). Recently, direct measurements of quantal release have been made from climbing fibers in the cerebellar cortex onto the closely apposed Bergmann glia (*3*). In spite of these findings there has been no demonstration of the participation of ectopic release of neurotransmitter in the course of inter-neuronal synaptic transmission.

At the structurally complex and umbrella-like calyceal synapse of the ciliary ganglion (CG) the case for ectopic release has been growing. Two major classes of kinetically distinct nicotinic acetylcholine receptors (nAChRs) are spatially segregated in the CG (*4, 5*, *6*). The α7-nAChRs are expressed on matted spines, but are largely excluded from PSDs regardless of where they occur (*7, 8, 9*). The α3*-nAChRs (*6*), are primarily localized to PSDs (whether on spines or somatic membrane), but present at lower density on non-PSD membrane (*4, 9, 10*). The α7-nAChRs exhibit profound desensitization, an order of magnitude faster decay time, and a 30-fold lower open probability compared to α3*-nAChRs (*11, 12, 13*).

The segregation of the two nAChR subtypes, especially the exclusion of α7-nAChRs from PSDs, has made it difficult to interpret physiological measurements that show the α7-nAChRs account for the majority of current in evoked EPSCs (*11, 12*), are necessary to sustain higher frequency throughput (*11*, *14*), and produce distinct Ca

signals localized to spines (*15*). Images of presynaptic vesicles within docking distance (ready to release), as well as Ω profiles (the image capture of fusing vesicles) are seen throughout the calyx including at loci far from PSDs (*4*). These findings have challenged the assumption that synaptic transmission is limited to traditional PSD associated AZs in the CG and suggests that neurotransmitter is released ectopically (*15*).

The unique geometry of the CG, combined with its specialized, molecular properties, is well suited to exploring detailed properties of synaptic transmission. Here, we introduce for the first time an accurate 3D model of synaptic topology with 9-nm resolution derived from electron tomography (*5, 16*) combined with Monte Carlo reaction/diffusion algorithms (MCell, http://www.mcell.cnl.salk.edu) that use 3D random-walk diffusion steps while tracking the probabilistic interactions of individual molecules governed by kinetic rate constants (*17, 18*, *19, 20, 21, 22, 23, 24, 25*). The model makes surprising predictions about the behavior of the two classes of nAChRs within functional microdomains as well as evidence that synaptic transmission in the CG requires ectopic neurotransmitter release.

Model Assembly. An MCell model is comprised of a description of the 3D geometry of the system along with molecule distributions and kinetics. Pre-and postsynaptic membrane surfaces were digitized from a 3D reconstruction of a CG spine mat derived from serial section electron tomography (4.4 nm/voxel) as described (*16*) and as applied to the CG (*4, 5, 29*). The pre- and postsynaptic membrane contours were first traced manually in each slice of the tomographic volume (Fig. 1A), and then transformed into triangle mesh surfaces (Figs. 1B, C) using the well-established marching cubes method from the field of computational geometry (*26*; Fig. S1). The postsynaptic surface

was segmented into PSD and non-PSD regions, populated with nAChRs and acetylcholinesterase (AChE), and associated with presynaptic vesicle release sites (Fig. 1D). A close-up of one release site (200 μs after ACh release) with many components is presented (Fig. 1E; distribution densities: α3*- nAChRs at 3600/μm^2 in PSD membrane and 80/μm^2 elsewhere (*10*); α7-nAChR at 3600/μm^2 on spine membrane only (*4*); the number of ACh molecules per vesicle is 5000 (*17*) and the density of AChE is 3000/μm^2 uniformly (*27*, *28*). Simulation with MCell requires that the structural model be annotated with reaction mechanisms, rate constants and spatial information regarding release sites and molecular components. These values were determined from published information (*29*; Fig. S2).

MCell counts the number of each molecular species in every state, after each Monte Carlo time step (1 μs here). Fig. 2A shows examples for the reaction of ACh with α3*- and α7-nAChRs in their various states - single-bound (red), double-bound closed (green), double-bound open (referred to as O-state henceforth) (black) and desensitized (blue; α7-nAChRs only).

Site-Dependent mEPSC Variability. Several vesicular release sites were chosen as simulation cases encompassing a variety of receptor subtype configurations and spatial geometries (Fig. 2B). One hundred trials were performed at each site. A composite of the averaged O-state response illustrates the wide variety of mEPSCs predicted according to the relative contributions of α3*- and α7-nAChRs and their spatial location (Fig. 2C). (It is curious that the amplitudes of responses at both PSD sites (1 and 2) differ by a factor of 2; the difference being that site 2 is surrounded by α7-nAChRs (see below)).

Model Sensitivity. We determined the sensitivity of our CG model to individual parameters. Based on their predominant receptor environments, site 1 was selected for α3*-nAChR and site 5 for α7-nAChR simulations. There was no sign of response saturation up to the maximum of 20,000 ACh molecules per quantum suggesting additional ligand capacity in the system (Fig. 3A). The α3*-nAChR response was more sensitive to ACh than that of α7-nAChRs. The manipulation of K_+ as an independent variable showed the original α3-nAChR K_+ lies in the relatively insensitive, low part of the curve, whereas the original K_+ for α7-nAChRs is located in the steepest part of the curve (Fig. 3B). Responses to α3*-nAChRs are more sensitive to changes in their respective receptor density than are α7-nAChR responses (Fig. 3C), but both exhibit residual capacity. The original density value for AChE lies at an efficient point (more AChE would not greatly reduce cleft ACh) (Fig. 3D). Although the simulated transient mEPSC events were far from equilibrium, the data (Fig. 3 A-D) were fit with equations derived from the equilibrium reaction mechanisms for the α3*- and α7-nAChRs as a benchmark (*29*, *30*).

We quantified the effects of individual parameter changes on model output by taking the first derivative (*f'*) – a measure of rate of change- of the curves from the sensitivity analysis at the point representing original conditions. In order to create a general measure of sensitivity suitable for cross comparison, we normalized the derivatives by multiplying by the ratio of the x- and y-axis values corresponding to the same point (*f'*-norm=$(f')(x_o/y_o)$). The unitless *f'*-norm values for α3*-nAChRs (with respect to ACh, AChR, AChE, and K^+) were 1.88, 0.91, -0.42, 1.48; and for α7-nAChRs

were 1.34, 0.69, -0.38, and .85, suggesting the model was most sensitive to changes in number of ACh molecules per quantum.

Population mEPSC Responses. To simulate population mEPSC responses, we programmed our model for 100 releases at each of 550 sites that represented vesicles within 5 nm (docking distance) of the presynaptic membrane in tomographic reconstructions of our CG volume (*5*). The peak mean open channel response for α3*-nAChR responses was 1.3 channels (Fig. 4A) and that for α7-nAChR responses was 2.13 channels, including 45 failures (Fig. 4E). Frequency histograms showing the distributions for the peak open channels, as well as the rise (20-80%) and fall times (τ), were also constructed for α3*- (Figs. 4B-D) and α7-nAChRs (Figs. 4F-H). Differences in the distributions including skew, median and tightness reflect variations in, and importance of, spatial domain (Figs. 2, 5) and kinetic properties.

If one assumes a single channel conductance of 68 pS for α7- and 37 pS for α3*-nAChRs (*13*), then the corresponding mean mEPSC amplitudes at a holding potential of -60 mV would be approximately 9.43 pA and 2.9 pA, respectively. The total mean mEPSC amplitude recorded in situ is 33 pA ± 0.7 at -60mV with a range between 5 and 80 pA (*11*). When adjusted with a detection threshold of 3 pA, all α3*-nAChR responses in the histogram distribution below 1.36 open channels (201 out of 550 or 36.5%) would go undetected and the new mean would rise by 50% from 1.3 to 1.95 open channels or 4.3 pA and close to the 8.4 pA mean recorded in situ in the presence of the selective α7-nAChR antagonist α-Bgt (*11*). Similarly, all α7-nAChR O-state responses below 0.73 (145 out of 550 or 26.4%) would not be measured, raising the mean by 34% from 2.13 to 2.85 or 11.7 pA. Assuming α3*-nAChRs contribute 8.4 pA, in situ, α7-nAChRs should

contribute about 24.6 pA. Thus, the true mean mEPSC amplitude is predicted to be two-thirds to three-quarters the size of that measurable experimentally.

Local Interactions between nAChR Subtypes. In order to visualize the spatial distribution of the mEPSC population, the location of each release site was mapped onto the postsynaptic surface of our model volume, and the radius of a sphere marking each site was scaled in proportion to the corresponding mean O-state response amplitude (Fig. 5A). It was observed above that the α3*-nAChR O-state amplitude at site 2 was half that of site 1 (Fig. 2C), even if both were PSD release sites, suggesting an effect of α7-nAChRs on α3*-nAChR O-state around site 2. The population of 550 mEPSC simulations was re-examined with the α7-nAChRs turned off (blockade of α7-nAChRs) and the α3*-nAChR mEPSC amplitudes (number of open channels) were compared in the two conditions by subtraction (without α7-nAChRs – with, Fig. 5B, left panel) and by percent increase (Fig. 5B, right panel). Positive changes are represented by yellow spheres and negative differences by cyan. The net effect of blocking α7-nAChR activity is an increase in the mean α3*-nAChR mEPSC amplitude from 1.27 to 1.36 open channels, a 7% rise (Fig. 5C, left panel). Responses gaining the most absolute amplitude were located on PSDs. The lack of cyan spheres over PSD areas that are surrounded by α7-nAChRs emphasizes the local interactions between the two nAChR subtypes (Fig. 5B, left panel). The locations of responses that exhibited the largest percentage increase in amplitude were regions where the smallest α3*-nAChR mEPSCs are normally produced (usually from non-PSD spine-regions, Fig. 5B, right panel). When we imposed a 3 pA detection threshold on the data, the mean α3*-nAChR mEPSC amplitude paradoxically declines 12% from 1.95 to 1.74 open channels (Fig. 5C, right panel). Under

this condition, the number of measurable α3*-nAChR mEPSCs increases (from 347 to 423), but most of these newly observable mEPSCs are low amplitude events that reduce the mean.

Testing the prediction of ectopic release. The mechanism of activation of extra-synaptic receptors (primarily α7-nAChRs) that contribute significantly to the evoked synaptic response have been debated (*31, 3, 11*, *12*, *14*). In our population mEPSC simulations we released vesicles at pan-calyceal sites (both PSD and ectopic) based on the observation that synaptic vesicles are widely distributed in the CG presynaptic terminal within 5 nm of the release face membrane (*5*). Thus far, we have kept the size of the vesicles uniform in order to better understand the effect of location and local geometry on synaptic response.

In addressing the issue of ectopic release, however, it was necessary to compare a simulated mEPSC data set to that recorded from CG in situ (*11)* a model refinement calling for a better estimate of vesicle size distributions. We measured synaptic vesicle lumen diameters from the reconstructed 3D tomographs (*29*; mean = 49.0 nm ± 6.0; Fig. 6A). This new distribution of vesicles (Fig. 6B) was adjusted volumetrically for the mean number of ACh molecules required to align our simulated mean mEPSC amplitudes with those from CG recordings (*11*). We cannot conclude, however, the actual number of molecules of ACh/vesicle without further experiments.

A new mEPSC population was created by sampling the distributed vesicle population 100 times for each of the 550 release sites (Fig. 6C, D). mEPSCs from ectopic and PSD regions were considered separately and together (pan-calyx) when expressed as cumulative probability plots and compared to the results from whole-cell recordings.

Additional simulations that included α7-nAChRs (with α3-nAChRs) in the spine PSDs, at an equivalent density to non-PSD areas, was also included to determine the impact of the PSD-exclusion of these receptors (Fig. 6E). A 6 pA detection threshold was applied to the simulated data, reflecting the recording conditions (*11*). Visual inspection of these data suggested a closer fit by either ectopic-only or pan-calyx events than by PSD-only or desegregated mEPSCs. The PSD-only population features a higher proportion of larger amplitude mEPSCs.

In order to quantitatively assess ectopic release contributions, distinct simulated mEPSC populations were generated by varying the fraction of vesicles released over PSDs (i.e. 1- ectopic fraction) and by varying the mean number of ACh molecules per quantum. The fraction of PSD vesicles was varied from 0 (i.e., 0% PSD vesicles and 100% ectopic) to 1 (i.e. 100% PSD and 0% ectopic). Simultaneously, the mean number of ACh molecules per quantum was varied from 5000 to 15000. The goodness-of-fit of each of these populations when compared to the population of experimentally recorded mEPSCs (*11*) was measured by the Kolmogorov-Smirnov test. The p-value of the goodness-of-fit is shown in gray-scale on the plot (Fig. 6F; lighter gray indicates better fit). This analysis demonstrates that mEPSC distributions with a high fraction of ectopic-released vesicles best match the recorded data.

Extrasynaptic receptor activation. The impact of spatial-kinetic interactions on principal events in the course of synaptic transmission including neurotransmitter spillover and the significance of extrasynaptic receptors is unclear (e.g., *32*, *33*, *34*). We addressed the question of ectopic vesicle release in the CG by quantitative comparison of the distributions of our simulated population of mEPSCs to those previously recorded

from intact CGs (*11*). We concluded ectopic vesicle release is likely the dominant component of synaptic transmission in the CG. The best fit to nearly 0% PSD release is a likely result of variations with model parameter values; any uncertainties could change the quantitative outcome (percentage of allowable PSD-release), but would not change the qualitative conclusion of a substantial ectopic release requirement.

Awareness of the important role of ectopic release at synapses is growing and challenging long-standing notions about synaptic structure and function (*3*). The function of non-PSD release in the CG specifically is probably closely linked to the specialized properties and function of α7-nAChRs, with their unique kinetics (*11*) calcium signals (*15*) and gene regulation (*35*). In future experiments, an analysis of the kinetic properties of the mEPSCs recorded from intact CG as well as the effects of non-uniform release probabilities will be incorporated into the model.

Sensitivity Analysis. The source of mEPSC distribution variability has been attributed variously to the size of synaptic vesicles and the concentration of agonist in the cleft (*25, 30, 36*), the density of postsynaptic receptors (*37*), the release site location or local environment (*36*) and stochastics of receptor flickering (*18*). Our model CG is most sensitive to the number of ACh molecules released into the cleft, implicating vesicle size as the primary source of variability (see normalized derivative sensitivity above; Fig. 3). The relative insensitivity of the O-state for nAChRs to variations in AChE densities in the vicinity of empirical measurements echoed those findings of previous Monte Carlo simulations in spatially synthetic conditions (*19, 20*).

Functional microdomains. Our results indicate that a single quantum of ACh is able in most cases to reach some α7-nAChRs, consistent with reports indicating that both

spontaneous and evoked synaptic responses are known to be mediated by both receptor types (*11, 12, 14*). In the case of site 1 (Fig. 2B), a somatic PSD release site, there was very little contribution of nearby spine-bound α7-nAChRs, suggesting a functional radius of around 0.2 μm for ACh in this CG model synapse. Population simulations similarly predict that the amplitude of mEPSCs generated by α3*-nAChRs at a PSD is greater when there are no surrounding α7-nAChR; the magnitude of the ACh sequestering effect of α7-nAChRs thus depends on the location of ACh release relative to nAChR distributions (Fig. 5B).

Our finding that α7-nAChRs buffer the availability of ACh for binding to α3*-nAChRs suggests a role for spatial organization in determining intrinsic synaptic variability (*18, 23, 25, 30*, *38*). A similar, cleft-limited diffusion buffering has been observed at snail synapses in culture where the extracellular glial-derived ACh binding protein modulates synaptic transmission by competing for released ACh (*39, 40*). Receptor interactions do not appear to be the case in a recent Monte Carlo model of central glutamatergic synapses where the proximity of NMDA and AMPA receptor subtypes to each other does not have an affect on channel openings (*24*).

Conclusion. The computational model synapse strongly supports the ectopic release of synaptic vesicles as the predominant mechanism of activation of extrasynaptic α7-nAChRs at CG synapses. This conclusion makes sense given the limited effective ACh diffusion radius, the kinetic disparities between nAChR subtypes and the principal contribution of the extrasynaptic, spine-bound α7-AChRs to many physiological measurements. The Kolmogorov-Smirnov analysis (Fig. 6F) verifies that in situ mEPSC distributions cannot be explained by traditional release patterns.

References

1. D. Zenisek, J.A. Steyer, W. Almers, *Nature* **406**, 849 (2000).

2. D. Lenzi, J.W. Runyeon, J. Crum, M.H. Ellisman, W.M. Roberts, *J. Neurosci*. **19**, 119 (1999).

3. K. Matsui, C.E. Jahr, *Neuron* **40**, 1173 (2003).

4. R.D. Shoop, M.E. Martone, N. Yamada, M.H. Ellisman, D.K. Berg, *J. Neurosci.* **19**, 692 (1999).

5. R.D. Shoop, E. Esquenazi, N. Yamada, M.H. Ellisman, D.K. Berg, *J. Neurosci.* **22**, 748 (2002).

6. W.G. Conroy, D.K. Berg, *J. Biol. Chem*. **270**, 4424 (1995).

7. M.H. Jacob, D.K. Berg, *J. Neurosci*. **3**, 260 (1983).

8. R.H. Loring, L.M. Dahm, R.E. Zigmond, *Neuroscience* **14,** 645 (1985).

9. H.L. Wilson Horch, P.B. Sargent, *J. Neurosci*. **15***,* 7778 (1995).

10. J.F. Margiotta, D.K. Berg, V.E. Dionne, *J. Neurosci*. **7**, 3612 (1987).

11. Z.W. Zhang, J.S. Coggan, D.K. Berg, *Neuron* **17**, 1231 (1996).

12. E.M. Ullian, J.M. MacIntosh P.B. Sargent, *J. Neurosci*. **17**, 7210 (1997).

13. M.E. McNerney, D. Pardi, P.C. Pugh, N. Qiang, J.F. Margiotta, *J. Neurophysiol*. **84**, 1314 (2000).

14. K.T. Chang, D.K. Berg, *J. Neurosci*. **19(**, 3701 (1999).

15. R.D. Shoop, K.T. Chang, M.H. Ellisman, D.K. Berg, *J. Neurosci*. **21**, 771 (2001).

16. G.E. Soto, et al., *Neuroimage* **1**, 230 (1994).

17. T.M. Bartol, Jr., B.R. Land, E.E. Salpeter, M.M. Salpeter, *Biophys. J.* **59**, 1290 (1991).

18. D.S. Faber, W.S. Young, P. Legendre, H. Horn, *Science* **258**, 1494 (1992).

19. L. Anglister, J.R. Stiles, M.M. Salpeter, *Neuron* **12**, 783 (1994).

20. M.R. Bennett, L. Farnell, W.G. Gibson, N.A. Lavidis, *Biophys. J.* **72**, 1595 (1997).

21. J.R. Stiles, T.M. Bartol, H.L. Fernandez, E.E. Salpeter, M.M. Salpeter, *Proc. Natl. Acad. Sci. USA*. **93**, 5747 (1996).

22. J.R. Stiles, I.V. Kovyazina, E.E. Salpeter, M.M. Salpeter, *Biophys. J*. **77**, 1177 (1999).

23. J.R. Stiles, T.M. Bartol, Jr., in *Computationl neuroscience: realistic modeling for experimentalists*, E. de Schutter, Ed. (CRC Press, 2001). pp. 87-127.

24. K.M. Franks, T.M. Bartol, T.J. Sejnowski, *Biophys J*. **83,** 2333 (2002).

25. K.M. Franks, C.F. Stevens, T.J. Sejnowski, *J Neurosci*. **23***,* 3186 (2003).

26. W.E. Lorensen, H.E. Cline, *Computer Graphics* **21**, 163 (1987).

27. J.Y. Couraud, H.L. Koenig, L. Di Giamberardino, *J. Neurochem*. **34,** 1209 (1980).

28. M. Vigny, S. Bon, J. Massoulie, F. Leterrier, *Eur. J. Biochem*. **85**, 317 (1978).

29. Materials and methods are available as supporting material on *Science* Online.

30. P. J. Kruk, H. Korn, D.S. Faber, *Biophys. J*. **73**, 2874 (1997).

31. D. Nguyen, P.B. Sargent, *J. Comp. Neurol*. **448**, 128 (2002).

32. J.S. Diamond, *J. Neurosci*. **21**, 8328 (2001).

33. D.A. DiGregorio, Z. Nusser, R.A. Silver, *Neuron* **35,** 521 (2002).

34. A. Momiyama, et al., *J. Physiol. (Lond.)* **549,** 75 (2003).

35. K.T. Chang, D.K. Berg, *Neuron* **32***,* 855 (2001).

36. M. Frerking, S. Borges, M. Wilson, *Neuron* **15**, 885 (1995).

37. Z. Nusser, S. Cull-Candy, M. Farrant, *Neuron* **19**,697 (1997).

38. H. Taschenberger, R.M. Leao, K.C. Rowland, G.A. Spirou, H. von Gersdorff, *Neuron* **36**, 1127 (2002).

39. A.B. Smit, et al., *Nature* **411**, 261 (2001).

40. K. Brejc, et al., *Nature* **411,** 269 (2001).

41. Supported by: State of California TRDRP (JSC); NSF (IBN-9985964, TJS, TMB, JRS); HHMI (TJS); NPACI NSF-ASC 97-5249 (TJS, TMB, MHE, MEM); NIH NCRR RR04050 (MHE, MEM); Human Brain Project DC03192 (MHE, MEM); and NIH NS12601 & NS35469 (DKB). We thank Drs. Peter B. Sargent and Charles F. Stevens for guidance and Dr. Rex Kerr for advice.

Supporting Online Material

Supporting Online Material

www.sciencemag.org

Materials and Methods

Figs. S1, S2, S3

Movie S1

Figure Legends

Fig. 1. 3D Model Reconstruction. **A**) Cross-sectional view approximately half-way through the middle of an E15 chick CG acquired with serial EM tomography and visualization software AnalyzeAVW. Several somatic spine cross-sections are seen along with vesicles packed in the presynaptic calyx. **B**) Same panel as in A with presynaptic and postsynaptic membranes traced in cyan and red, respectively, using Xvoxtrace. Scale bar = 0.5 μm **C**) Serial section reconstruction after the surface is reconstructed with the marching cubes algorithm. The presynaptic membrane (cyan) overlies postsynaptic membrane (red). **D**) Viewed with DReAMM, the MCell compatible model, complete with all previously reported PSDs (shown as black circular regions). Postsynaptic spine mat membrane is light blue, while somatic membrane is gray. Area within white box enlarged in next panel. **E**) Close-up view of MCell compatible model. Yellow sphere represents synaptic vesicle. Green ovoids represent ACh molecules. Translucent blue squares and red circles represent α7- and α3*-nAChRs, respectively. Opacity of nAChR color corresponds to level of receptor activation (fully opaque = open channel) 200 μs after ACh release. Scale bar = 0.1 μm.

Fig. 2. MCell output and location effects. **A**) Time course of α3*- and α7-nAChR channel states after release of a single quantum. Green = double-bound closed (C2); black = double-bound open (O); red = single-bound (C1); blue = desensitized (C3, α7-nAChRs only). See *29* and fig. S2 for mechanisms and states. Scaling differences require presentation in two panels per receptor-type (top and bottom). **B**) Site map of selected release sites representing the greatest range of nAChR distributions. Vesicles are released at numbered yellow spheres indicated with white arrows, PSDs indicated by

black-shaded patches, spine membrane blue, somatic membrane gray. Scale bar = 0.5 μm **C)** O-state responses (mean of 100 trials) from 5 sites in **B.**

Fig. 3. Model sensitivity. The effects of modulating the levels of four model components on O-state. **A**) Effect of number of ACh molecules per quantum (original condition: n = 5000 on O-state for α3*- and α7- nAChRs (fit: r = 0.999, α3*; r= 0.998, α7). **B**) Effect of varying the K_+ on O-state for α7- and α3*-nAChRs. Original values for α7-nAChR K_+ = 4.1 x 10^7 $M^{-1}s^{-1}$; and for α3*-nAChR K_+ = 2.3 x10^6 $M^{-1}s^{-1}$(fit: α3*, r =0.999; α7, r = 0.987). **C**) Effect of changing α3*- and α7-nAChR receptor density on O-state. Original value for both nAChRs was 3600/μm^2 (fit: α3*, r = 0.992; α7, r = 0.986). **D**) Effect of AChE density on O-state. Original AChE density in model was 3000/μm^2 (fit: α3*, r = 0.997; α7, r = 0.995). All values in all panels are mean ± S.D., n = 100 per point. Arrows indicate original model values for each receptor type.

Fig. 4. Simulated population mEPSC analysis. **A**) cumulative mean O-state α3*-nAChR mediated mEPSC. Histograms of **B**) mean number of peak open channels (bin = 0.075; same x-axis scale as (F) for comparison); inset is the expanded full x-axis scale **C**) rise times (bin = 10); and **D**) fall times (bin = 0.25). **E**) cumulative mean α7-nAChR mediated mEPSC (including 45 failures). Histograms of **F**) open channels (bin = 0.076); **G**) rise times (bin = 3); and **H**) fall times (bin = 0.015).

Fig. 5. Spatial mapping of mEPSCs and functional microdomain effects. **A)** 550 vesicle sites with equal probability of release simulate a population of mEPSCs. Mean response (100 trials each) was mapped by the corresponding release location on the postsynaptic surface, vesicle radius (yellow spheres) are scaled to the open channel

amplitude of the mEPSC. The maps are segregated for each type of nAChR (α3*- left, α7- right). **B)** Maps of the difference in α3*-nAChR mEPSC amplitudes with and without α7-nAChRs (left panel), and the percent change in α3*-nAChR mEPSC amplitude without α7-nAChRs (right panel). Yellow = positive and cyan = negative changes. **C)** Mean α3*-nAChR mEPSC responses in the presence (black trace) and absence (red trace) of α7-nAChRs (left panel); and with (black) and without (red) α7-nAChRs after a 3 pA detection threshold.

Fig. 6. Examination of ectopic release. **A**) Frequency distribution of synaptic vesicle lumen diameters measured from tomographic reconstruction. **B)** Vesicle size distribution adjusted volumetrically for ACh content. Mean number of ACh molecules (10,000) is that required to match the mean mEPSC amplitude from experimentally recorded events (*11*). **C**) Population of mEPSCs from simulations with distributed vesicle sizes showing ectopic-only sites; **D)** Population of mEPSCs from simulations with distributed vesicle sizes showing PSD-only sites. **E)** Cumulative probability plots of mEPSCs from CG whole-cell recordings (dotted line, *11*) and mEPSCs for simulated ectopic-only (thick black), pan-calyx (middle thickness black), PSD-only release (thin black), and PSD-only with α7-nAChRs (gray line) populations **F)** Contour plot of goodness-of-fit between simulated and experimentally recorded mEPSCs. Distinct simulated mEPSC populations were generated by varying the fraction of vesicles released over PSD versus ectopic sites and by varying the mean number of ACh molecules per quantum. The fraction of PSD vesicles was varied from 0 (i.e., 0% PSD and 100% ectopic) to 1 (i.e. 100% PSD and 0% ectopic). The goodness-of-fit of each of these populations to the population of recorded mEPSCs (*11*) was measured by the

Kolmogorov-Smirnov test. The p-value of the goodness-of-fit is shown in gray-scale. Lighter gray indicates increasing similarity between the simulated and experimental populations. The outermost contour line indicates p=0.02 limit of confidence that the populations are dissimilar and the inner line indicates the p=0.05 limit.

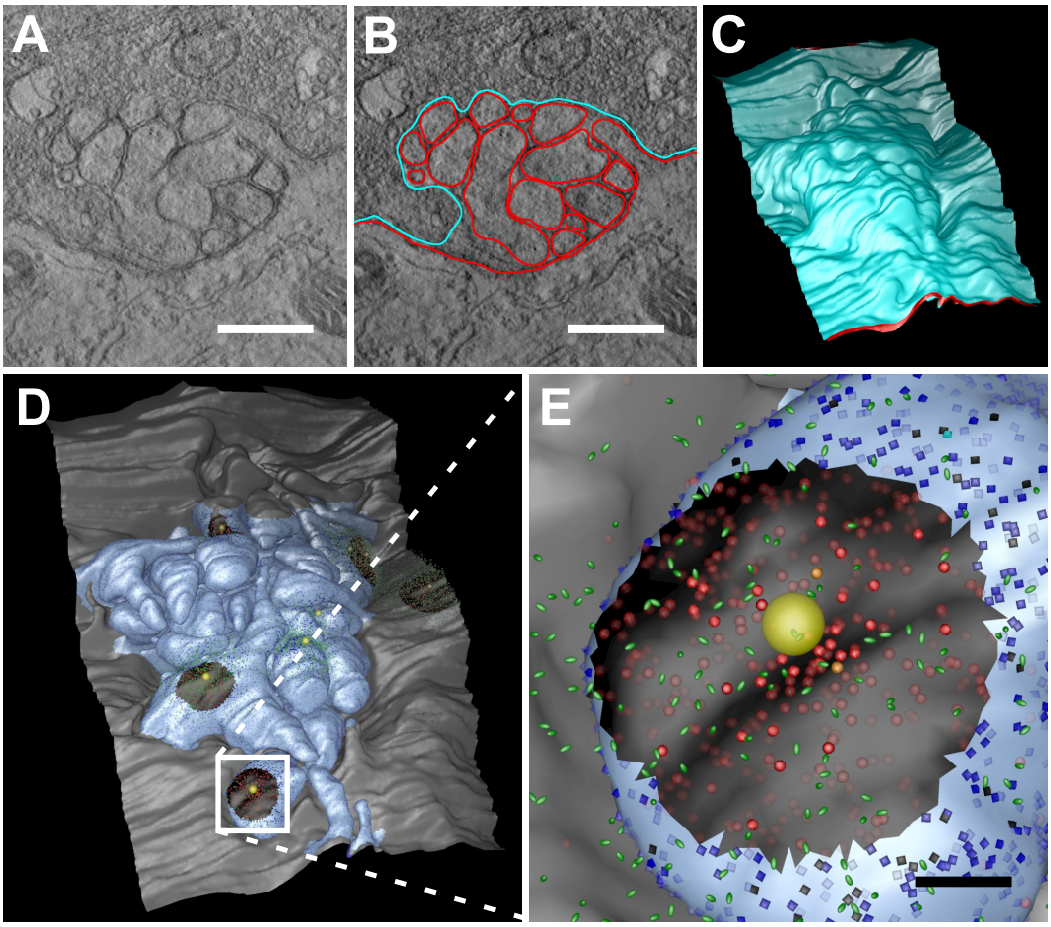

Figure 1

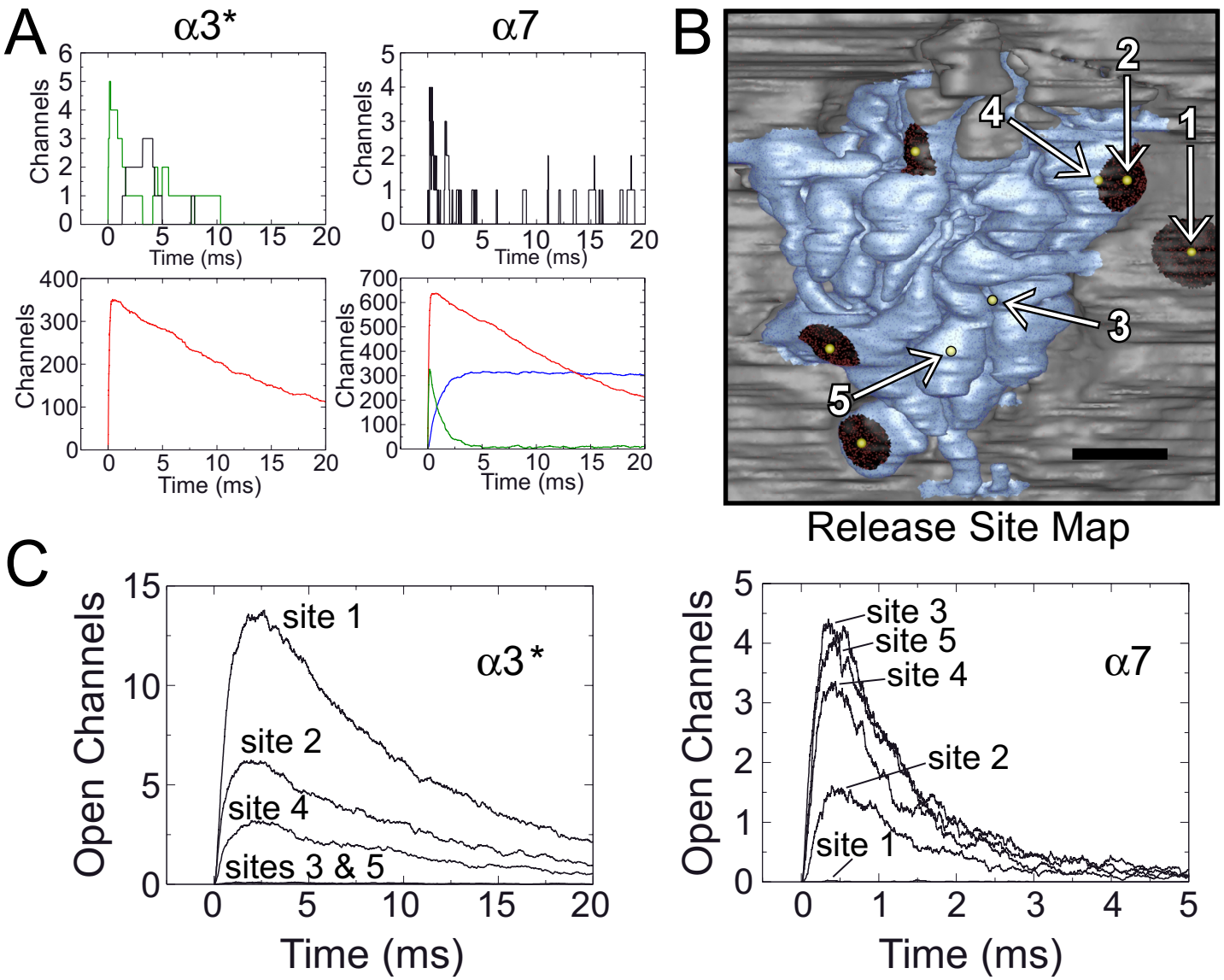
A
α3*
α7
Channels
Time (ms)
B
1
2
3
4
5
Release Site Map
C
Open Channels
Time (ms)
α3*
site 1
site 2
site 4
sites 3 & 5
α7
site 3
site 5
site 4
site 2
site 1

Figure 2

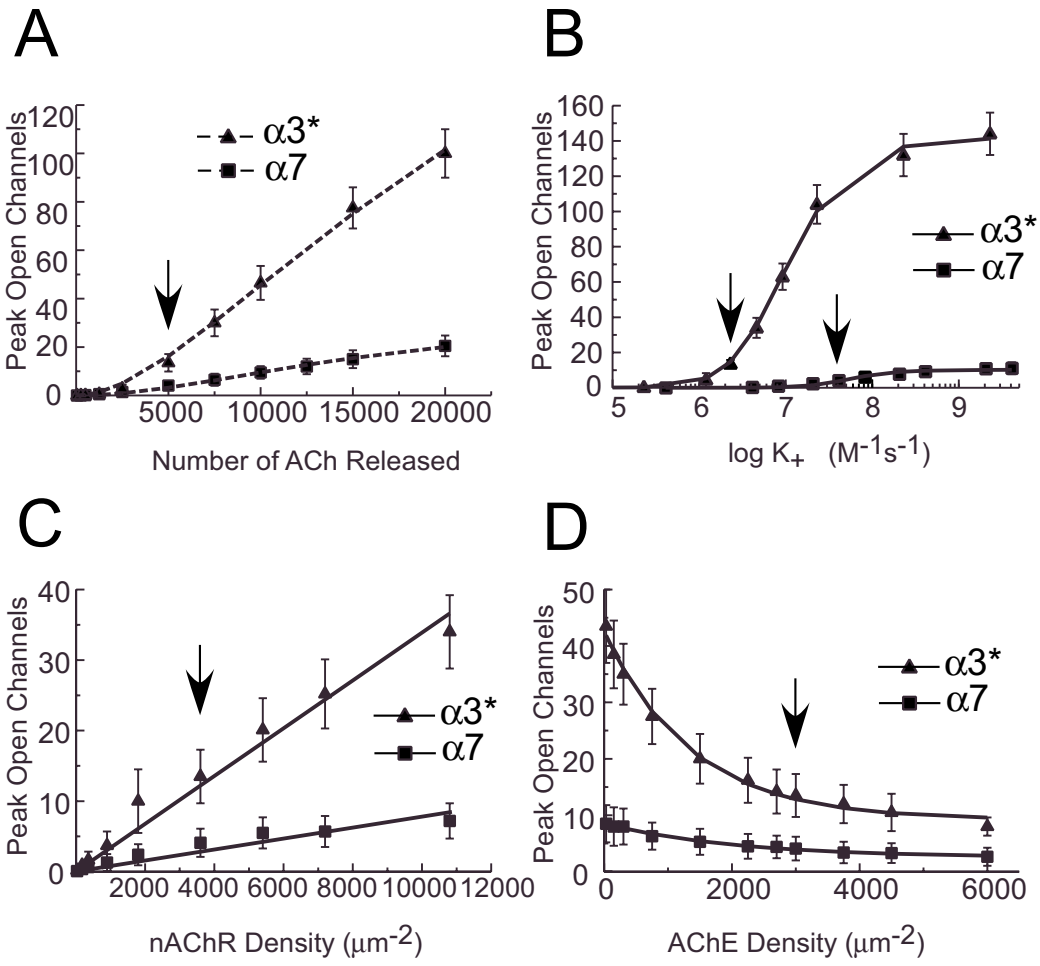
A
Peak Open Channels
120
100
80
60
40
20
0
α3*
α7
5000
10000
15000
20000
Number of ACh Released
B
Peak Open Channels
160
140
120
100
80
60
40
20
0
α3*
α7
5
6
7
8
9
log K+ (M-1s-1)
C
Peak Open Channels
40
30
20
10
0
α3*
α7
2000
4000
6000
8000
10000
12000
nAChR Density (μm-2)
D
Peak Open Channels
50
40
30
20
10
0
α3*
α7
0
2000
4000
6000
AChE Density (μm-2)

Figure 3

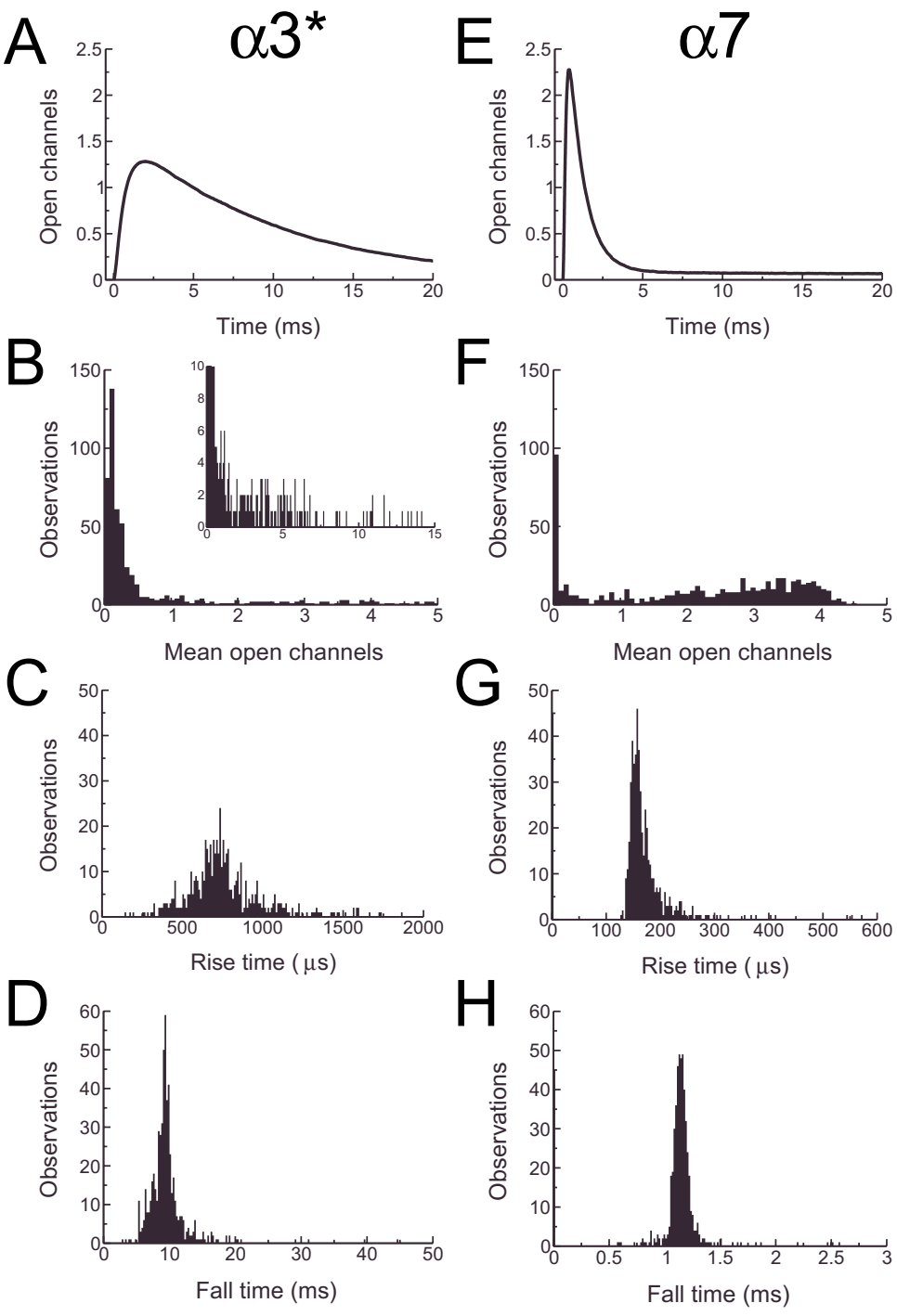
A
α3*
E
α7
Open channels
Time (ms)
B
F
Observations
Mean open channels
C
G
Rise time (μs)
D
H
Fall time (ms)

Figure 4

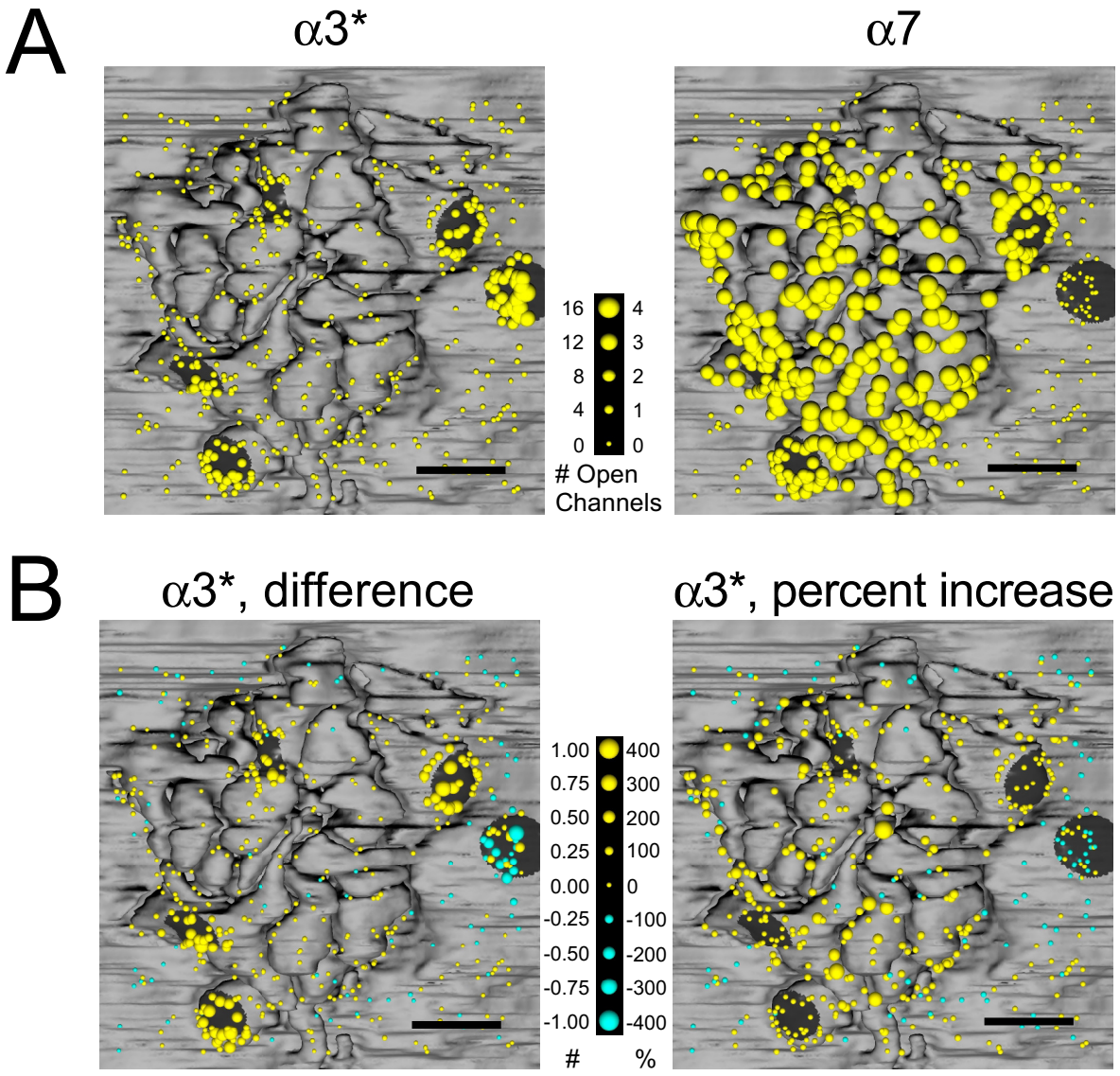
A
α3*
α7
16
12
8
4
0
4
3
2
1
0
Open Channels
B
α3*, difference
α3*, percent increase
1.00
0.75
0.50
0.25
0.00
-0.25
-0.50
-0.75
-1.00
400
300
200
100
0
-100
-200
-300
-400
#
%
C
no threshold
3 pA threshold
Open Channels
α3* with α7
α3* without α7
Time (ms)
0
0.5
1
1.5
2
5
10
15
20

Figure 5

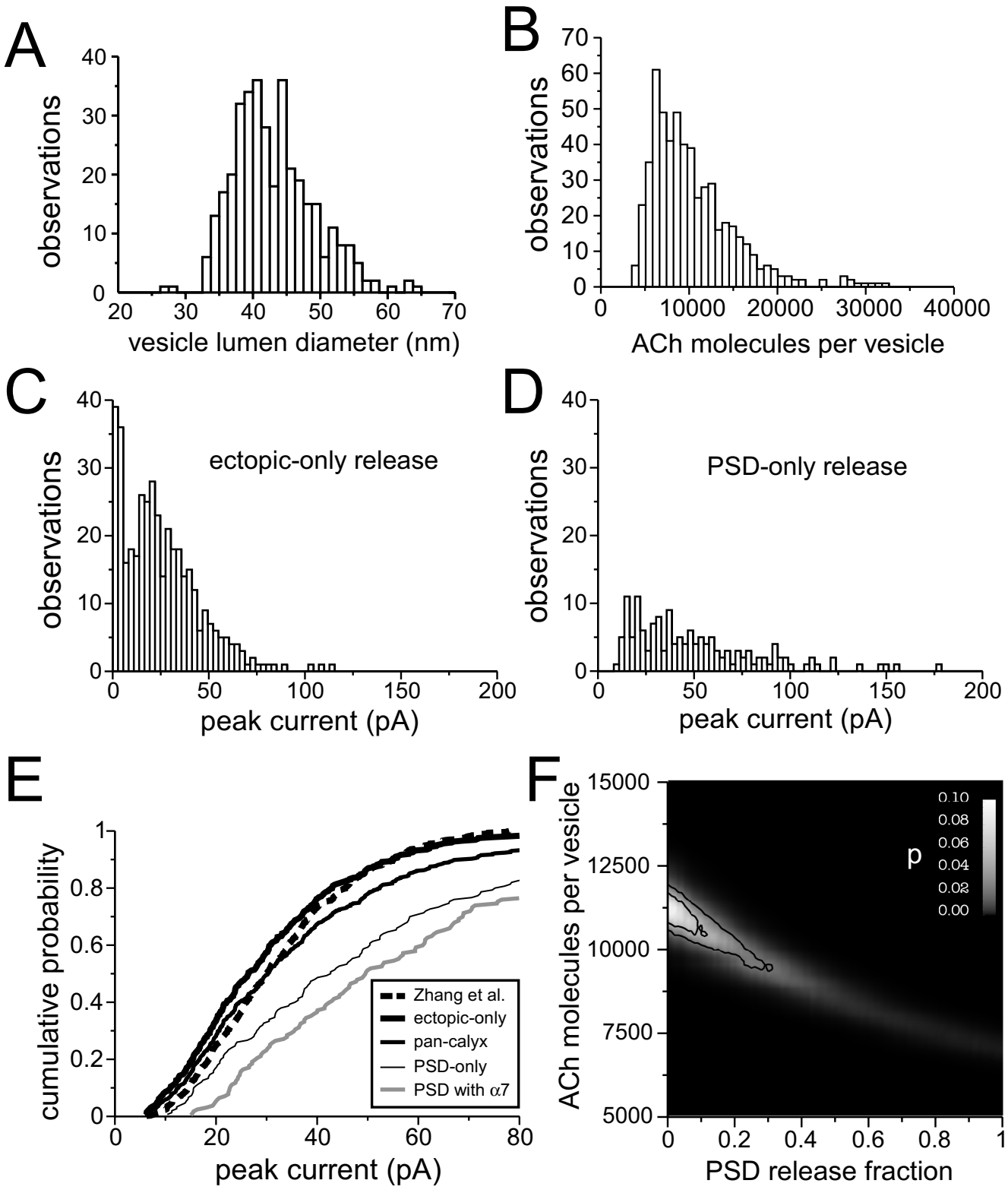
A
observations
vesicle lumen diameter (nm)
B
observations
ACh molecules per vesicle
C
ectopic-only release
observations
peak current (pA)
D
PSD-only release
observations
peak current (pA)
E
cumulative probability
peak current (pA)
Zhang et al.
ectopic-only
pan-calyx
PSD-only
PSD with α7
F
ACh molecules per vesicle
PSD release fraction
p
0.10
0.08
0.06
0.04
0.02
0.00

Figure 6

Supporting Online Material

Materials and Methods

Sample Preparation and Serial EM Tomogram Reconstruction. The procedures for creating the serial EM tomogram reconstruction of the portion of the chick CG calyceal synapse used in this study have been previously described (*1*, *2*). Six serial 1 μm thick EM tomogram volumes were combined into one contiguous volume. Inspection of the volume with Xvoxtrace (software developed by S. Lamont, National Center for Microscopy and Imaging Research) showed that a complete spine mat was encompassed by a 640x640x690 voxel (2.8 x 2.8 x 3.0 μm) subvolume of the complete tomogram (4.4 nm/voxel).

The approach for aligning and joining sections is described in detail in (*3*). Briefly, volumes containing specimen material were extracted from each section adjusted for differences in the tip and tilt while doing a best fit of the uppermost slice of one section with the bottommost slice from the one it was being joined to. Warping to compensate for the beam-induced mass loss or differences in orthomorphic compression during sectioning were not done. The sections aligned well enough to follow the surfaces of the synaptic components and to make a continuous model suitable for the simulations. The actual construction of these ciliary ganglion models from serial electron tomograms has been described (*1*).

Spine Mat Membrane Reconstruction. To produce a continuous and accurate surface model of the pre- and postsynaptic membranes (and therefore the cleft space), we traced the 690 sections of the tomogram manually in Xvoxtrace. Typical tracings of the

pre- and postsynaptic membranes are shown as cyan and red contours, respectively, in Fig. 1A. Note that the spinous topology of the postsynaptic membrane results in apparently disjoint membrane contours (especially for the postsynaptic membrane) in a typical 2D slice through the volume.

The set of pre- and postsynaptic membrane contours were then reconstructed into a triangle mesh surface representation (Fig. 1B, C) using the well-established computational geometry method called marching cubes 3D surface construction (*4*). We used the marching cubes function found in the Visualization Tool Kit (VTK, http://www.kitware.com/). The two triangle meshes obtained from this step were composed of ~2 million and ~6 million triangles for the pre- and postsynaptic membranes, respectively. The number of triangles required to represent each surface was reduced via decimation using the surface simplification tool in DReAMM (http://www.mcell.psc.edu/DReAMM/). Decimation of the postsynaptic surface with a 1% error criterion yielded ~300,000 triangles with a mean area of 664 ± 232 nm^2 and a total surface area of 199 μm^2. Decimation of the presynaptic membrane resulted in ~20,000 triangles with a mean area of 698 ± 183 nm^2 and a total surface area of 14 μm^2.

Labeling Postsynaptic Surface Regions. Once a model was obtained the appropriate densities and distributions of receptor and enzyme molecules were placed on the postsynaptic membrane. This entailed labeling the regions of this surface corresponding to the PSD and spine regions already identified (*1, 2*). A total of 14 spines were isolated to allow further manipulation (Fig. S1). It is important to note that regions of mesh representing the individual spines had to be isolated from each other and from the rest of the postsynaptic membrane without altering the coordinates of the triangles as

this would disrupt the integrity of the surface. To accomplish this, a bounding 3D "lasso" for each spine was created in 3 steps: 1) the entire postsynaptic membrane object was exported from Xvoxtrace as a volume in which the intracellular space was filled with white voxels and the extracellular space filled with black voxels (Fig. S1A); 2) A volume of space to be isolated representing, for example, an individual spine, was removed from the whole volume by erasing the surrounding area in all 690 slices of the volume (Fig. S1B); 3) the resulting volume containing just a single spine was then reconstructed as a closed, bounding surface just larger than the actual spine surface using the VTK marching cubes method by specifying an isocontouring level just outside the actual spine surface (Fig. S1C). In this way, a form-fitting bounding surface was obtained that could serve as a 3D lasso to isolate the individual spine from the postsynaptic surface. All whole triangles in the postsynaptic surface fully enclosed by the lasso surface were extracted and copied to a separate mesh file – this file now contained the unmodified triangles representing an individual spine as required. This process was repeated for each of the 14 spines.

The spines were taken individually and populated with a high density of α7-nAChRs and a low density of α3*-nAChRs. All 5 PSDs previously identified in this tomogram (*1, 2*) were defined on the spine and non-spine membranes using the probe tool in DReAMM (Fig. S1D). The PSDs were populated with a high density of α3*-nAChRs. After all the receptor sites were defined in their subcellular locales, the spines and the postsynaptic membrane were reassembled (Fig. 1D)

Specification of Release Sites. Two different methods were used to place neurotransmitter release sites in the model. In the first placement method, several

specific sites of synaptic vesicle release were chosen and placed approximately at the level of the presynaptic membrane. These sites were chosen as representative of the variability in site neighborhood including PSDs populated with only α3*-nAChRs and spine sites populated with mostly α7-nAChRs, as well as others with mixed populations (Figs. 1D and 2B). A close up view of one of the release sites at a PSD (black area) on a spine shows both populations of nAChRs (yellow spheres and blue diamonds, opacity correlates to activation state), the release vesicle (red sphere), and ACh molecules (cyan ellipsoids- not to scale) (Fig. 1E).

In the second site placement method, release sites were determined based on the distributions of synaptic vesicles from previously published serial EM tomograms (*1*). We assumed all vesicles located within 5 nm of the presynaptic membrane represented potential docking sites. A density estimate suggested the positioning of 550 release sites, randomly distributed throughout the model, but with a slightly higher density at the PSDs. Unless otherwise noted, each site was assigned an equal probability of release. The population of simulated mEPSCs also comes from a single spine mat. Our sample of neuronal surface, however, is likely to be representative of CG spine morphology and surroundings, based on additional reconstructions (*2*).

Computing Resources. Computer simulations were performed using MCell version 2.50 (http://www.mcell.cnl.salk.edu/) running on an NPACI Rocks Linux cluster (http://rocks.npaci.edu/Rocks/) of 2.8 GHz Intel Pentium 4 Xeon processors and a Debian Linux cluster of 1.8 GHz AMD Athlon MP processors. MCell parameter sweep runs were performed using APST version 2.20 (http://grail.sdsc.edu/projects/apst/). Each

individual MCell run required ~400MB of RAM and took ~45 seconds of CPU time on a single processor.

Fitting Data. Equations describing the activation of α3* and α7-nAChRs were derived from their corresponding equilibrium reaction schemes (see Fig. S2A).

For the α3*-nAChR:

$$O = \frac{C}{\frac{K_-^2 \alpha}{([A]K_+)^2 \beta} + \frac{2K_- \alpha}{[A]K_+ \beta} + \frac{\alpha}{\beta} + 1} \qquad \text{(Equation 1)}$$

For the α7-nAChR:

$$O = \frac{C}{\frac{K_-^2 \alpha}{([A]K_+)^2 \beta} + \frac{2K_- \alpha}{[A]K_+ \beta} + \frac{K_{des}\alpha}{K_{res}\beta} + \frac{\alpha}{\beta} + 1} \qquad \text{(Equation 2)}$$

where O represents double-bound open AChRs and C equals the total number of AChRs. In both cases it was necessary to convert number of ACh molecules to concentration, represented by [A], with the following formula:

$$[A] = \frac{10^{15}\,\mu m^3 / L}{6.02x10^{23}} \left(\frac{x}{a_o^3 \mu m^3}\right) \qquad \text{(Equation 2b)}$$

where x is the number of ACh molecules in the simulation and a_0 is equal to the length of one side of the bounding box containing the concentration of ACh ([A]) and L means liter.

These equations describe a sigmoidal function consistent with theoretical predictions for the steady state. Although our dynamic synaptic simulations never reach steady state as in vivo, the basic form function of the transmitter concentration effect on state O is preserved (*5*).

The data from simulations with variable AChE densities were best fit with a single exponential equation with negative slope.

$$O = a_o e^{(-x/a_1)} + a_2 \quad \text{(Equation 3)}$$

The χ- function. The χ- function, which has been described earlier (*6*), was used to calculate K_{des} (desensitization constant) and K_{res} (re-sensitization constant) for α7-nAChR. Briefly, χ- is equivalent to the inverse of the time constant of the falling phase of the response (τ) and can be expressed in terms of the *total* reverse binding rate (K_{t-}) and the forward and reverse rate constants for the double-bound closed to double-bound open state transition (β and α).

$$\chi_{-} = \frac{1}{\tau} = \frac{\alpha 2K_{t-}}{\alpha + \beta + 2K_{t-}} \quad \text{(Equation 4)}$$

with

$$K_{t-} = \frac{2K_{-} + K_{des}}{2} \quad \text{(Equation 4b)}$$

The τ values for the α3* - and α7-nAChRs were assumed to be 40 ms and 1.1 ms, respectively (*7, 8, 9, 10*). The first step was to solve the equation for K_{des}. Then, in order to solve for K_{res}, the value for K_{des} was used as β, and the equation was solved for α which in this case becomes equivalent to K_{res}.

AChR and AChE Distributions. Distribution of α7-nAChRs were based on: 0.01 fmoles α-bgt binding/neuron (*11*) and 4 binding sites/receptor (*12*) gives 1.5 x 10^6 receptors/neuron; 13 spines/mat and 20 mats/ neuron (unpublished estimates; *1*),

assuming all α7-nAChRs on spines (*1*); average spine area = 1.6 μm^2 (*1*); above assumptions yield estimate of 3600 α7-nAChRs/μm^2 (number of α7-AChRs in the model = 84,729).

The distribution of α3*-nAChRs was determined assuming localization at PSDs with lower densities in non-PSD areas (*1*); approx. 10^5 receptors/neuron (*7*); approx. PSD area = 0.03 μm^2; estimate 5 PSDs/ spine mat (*1*); estimate 20 spine mats/cell (unpublished estimates, *1*); from above estimates we placed 3600 receptors/μm^2 of PSD membrane and 80 receptors/μm^2 non-PSD membrane, yielding 1.1 x 10^5 receptors/neuron (number of α3*-nAChRs in the model = 4,796). In the "Sensitivity Analysis" section, the range of nAChR densities were centered around, but extending both above and below, these original values (i.e., 0.1x, 0.25x, 0.5x, x, 1.5x, 4x, 10x).

Distributions of AChE were determined by assuming a turnover rate of 600 nmoles/hr in the ciliary ganglion (*13*), an AChE $K_+ = 1.5 \times 10^8\ M^{-1}s^{-1}$ (*13*); a AChE K_{cat} = 3571/s (*14*), and the equation:

$(6x10^{-7}$ moles/hr x $6x10^{23})/(9x10^6\ \mu m^2$ x 3600s/hr x 3571/s)= 3111/μm^2 (round to 3000).

The total number of AChE molecules in the entire model is 156,129. The kinetic scheme for AChE was assumed to be the same as at the neuromuscular junction (*15*). In the MCell simulation, when a molecule of ACh meets a molecule of AChE it binds with a

given binding constant and is hydrolyzed at the corresponding catalytic rate (above). When ACh collides with the sides of the model bounding-box enclosing the simulation, it disappears immediately.

Input Parameters. The reaction mechanisms for the two classes of nAChRs are based on muscle nAChR schemes (Fig. S2; *8*, *15*, *16*); the difference between them being the addition of a desensitization step for the α7-nAChR. Desensitization of α3*-nAChRs is more than an order of magnitude slower and is omitted from the scheme. The corresponding rate constants for each step in the reaction mechanisms are tabulated next to the reaction schemes in figure S2. The distributions of the nAChRs are also shown. The rate constant and distributions for AChE were $K_+ = 1.5 \times 10^8$ $M^{-1}s^{-1}$ (*13*) and $3000/\mu^2$, respectively. The diffusion coefficient for ACh was 2.1×10^{-6} cm^2/s (*17*) and number of molecules per vesicle was set at 5000.

Estimating the Forward Binding Rate (K_+) for the α7-nAChR. The rate constant with the least certainty is K_+ for α7-nAChRs. The K_+ (from $K_d=K_-/K_+$), depends on K_- measured from single-channel recording and K_d coming ideally from physiological experiments. Because of the rapid desensitization, however, it is experimentally difficult to apply agonist fast enough to get an accurate EC_{50} value (*18*), resulting in underestimates of the real potency or efficacy of agonist (*19*). Recently, it has been shown using net charge calculations that the true EC_{50} for α7-nAChRs is likely 10- fold lower than previously thought (*19*, *20*). We, therefore, used the K_d value from binding experiments to calculate K_+ for α7-nAChRs as 4.1×10^7 $M^{-1}s^{-1}$. Simulations using at a pure α7-nAChR site on a spine resulted in an average of 4.1 O-state channels, within the range observed in laboratory recordings (*7*).

In order to get a lower limit on a value for the α7-nAChR K_+ we used MCell simulations under special conditions. The maximum number of ACh molecules per quantum (originally set at 5000) was set to 20,000. The maximum density of α7-nAChRs (originally 3600/μm^2) was set to 12,000/μm^2 (*21*). Maximizing these variables allows us to find the minimum value of K_+ that will bring the system back to the same peak output response as the original simulation. Under these conditions we made the α7-nAChR K_+ an independent variable using a range of values over 4 orders of magnitude and produced a dose-response relationship for the new condition (Fig. S3A). The K_+ that now corresponds to approximately 4.1 open α7-nAChRs gives us the minimum K_+ for α7-nAChRs. This value was 2.0 x 10^6 $M^{-1}s^{-1}$. As an upper limit, we take the K_+ of AChE, one of the fastest enzymes known, with an order of 10^8 $M^{-1}s^{-1}$ for the forward binding constant. Our best estimate value of 4.1 x 10^7 $M^{-1}s^1$ lies between these two brackets.

Since information about K_+ can be gleaned from rise time analysis, we examined the α7-nAChR rise times (20-80%) using K_+ values ranging over four orders of magnitude (n=2-5 groups of 20 averaged trials each, except for point at 8.2 x 10^6 $M^{-1}s^{-1}$which is n=3 groups of 200 averaged trials). But because of the predominance of α and β in determining O-state transitions, there was no significant effect on rise times (Fig. S3B). Thus, these simulations could not improve our α7-nAChR K_+ estimate.

Saturation. The level of saturation in response to a single quantum varies with each nAChR (*22*). In the case of α3*-nAChRs in the isolated PSD (site 1), the receptor saturation level was 8.8%. The level of saturation is primarily determined by the K_+, the activity of AChE, amount of ACh and diffusion. For α7-nAChRs, the quantal efficacy

was calculated according to the saturated disk model (*22)* because of the non-limiting area occupied by α7-nAChRs on the spines. At site 5 on the spines this value was 15%.

Measuring Vesicle Diameters. The maximum diameter (longest of approx. 10 slice diameters per vesicle) of the vesicles in the reconstructed 3D tomograph were measured using Xvoxtrace from membrane midpoint to midpoint (6nm membrane thickness). In a total of 358 vesicles the mean diameter was 49.0 ± 6.0 nm implying a mean lumen diameter of 43.0 ± 6.0 nm. In the simulations, except where noted, vesicles were filled with a constant 260 mM ACh (corresponding to a mean number of approx. 10000 ACh molecules) (see Fig.6).

Figure Legends

Fig. S1. Using the Image Edit tool from the AnalyzeAVW software, the segmented postsynaptic microanatomy is separated from the rest of the volume. **A**) Shows the segmentation of the same section as shown in Fig. 1A but here white indicates the membrane edge and intracellular space of the postsynaptic structure. Scale bar = 0.5 μm. **B**) An individual spine in cross-section is further separated from the rest of the postsynaptic volume. **C**) The individual spine reconstructed using marching cubes and rendered as a 3D surface in DReAMM. **D**) Region tool (yellow sphere) of DReAMM being used to mark the approximate region of the PSD membrane (orange patch) on an excised spine.

Fig. S2. MCell input parameters. **A**) Reaction schemes, kinetic rate constants for CG α3*- and α7-nAChRs. **B**) Distributions for nAChRs.

Fig. S3. Parameter bracketing of the forward rate constant (K_+) for α7 nAChRs. **A**) Finding the lower envelope for α7-nAChR K_+. ACh and AChR densities were set to

theoretical maximum values (ACh per vesicle = 20,000; AChR density = 12,000/μm^2). The α7-nAChR K_+ was then varied over wide range. Dotted-line indicates number of channels open under original conditions (4.1) and the corresponding lowest likely K_+ for α7-nAChRs ($2x10^6$ $M^{-1}s^{-1}$). **B**) Rise time analysis for α7-nAChR O-state as a function of α7-nAChR K_+ and fitted; n=2-5 groups of 20 averaged trials each, except for point at 8.2 x 10^6 $M^{-1}s^{-1}$which is n=3 groups of 200 averaged trials.

References

1. R.D. Shoop, et al., *J. Neurosci*. **19**, 692 (1999).

2. R.D. Shoop, et al., *J. Neurosci*. **22**, 748 (2002).

3. G.E. Soto, et al., *Neuroimage* **1**, 230-243 (1994).

4. W.E. Lorensen, H.E. Cline, *Computer Graphics* **21**, 163-169 (1987).

5. P.J. Kruk, H. Korn, D.S. Faber, *Biophys*. *J*. **73**, 2874 (1997).

6. B.R. Land, et al., *Proc. Natl. Acad. Sci*. **81**, 1594 (1984).

7. Z.W. Zhang, J.S. Coggan, D.K. Berg, *Neuron* **17**, 1231 (1996).

8. J.F. Margiotta, D.K. Berg, V.E. Dionne, *J. Neurosci*. **7**, 3612 (1987).

9. E.M.Ullian, et al., *J. Neurosci*. **17**, 7210 (1997).

10. M.E. McNerney et al., *J. Neurophysiol*. **84**, 1314 (2000).

11. V.A.Chiapinelli, E. Giacobini, *Neurochem*. *Res*. **3**, 465 (1978).

12. Brejc, K., et al., *Nature* **411**, 269 (2001).

13. J.Y. Couraud, et al., *J. Neurochem* **34**, 1209 (1980).

14. M. Vigny, et al., *Eur*. *J. Biochem*. **85**, 317 (1978).

15. T.M Bartol, Jr., et al., *Biophys. J*. **59,** 1290 (1991).

16. A. Mathie, et al., *J. Physiol. (Lond.)* **439**, 717 (1991).

17. T. M. Bartol, PhD thesis, Cornell University (1992).

18. M.I. Glavinovic, H.R. Rabie, *Eur. J. Physiol*. **435**, 193 (1998).

19. R.L. Papke, J.S. Thinschmidt, *Neurosci. Lett*. **256**, 163 (1998).

20. R.L. Papke, J.K. Porter Papke, *Br. J. Pharmacol*. **137**, 49 (2002).

21. N. Unwin, *J. Mol. Biol*. **229**, 1101 (1993).

22. M.M. Salpeter, in *The Vertebrate Neuromuscular Junction* (Alan R. Liss Inc., New York, 1987), pp.-1-54.

23. P. Pugh, Ph.D. thesis, University of California, San Diego, 1995.

24. $K_{C0C1} = K_{+} = K_{-}/K_d$; using K_d = 36 μM, from 8.

25. $K_{C0C1} = K_{+} = K_{-}/K_d$; using K_d = 2 μM from 23.

26. Calculated from decay time constant (τ) of 10 ms for α3*-nAChR (refs. 7, 9, 10) using method of "effective unbinding rate" (6): $1/\tau = \chi_{-} = (\alpha 2K_t)/(\alpha+\beta+2K_{-})$, solving for K_{-} ($K_{-}=K_{C1C0}$).

27. Calculated from decay time constant (τ) of 1.1 for α7 using method of "effective unbinding rate" (see ref. 6): $1/\tau = \chi_{-} = (\alpha 2K_{t-})/(\alpha+\beta+2K_{-})$, solving for K_{t-}, then K_{des} (K_{C2C3}) = $2K_{t-} - 2K_{-}$ (where $2K_{-} = K_{C2C1}$). For K_{res}, use χ_{-} equation, with Kres = α, K_{des} =β, and using 4/s (or 250 ms) as resensitization τ (for χ_{-} equation).

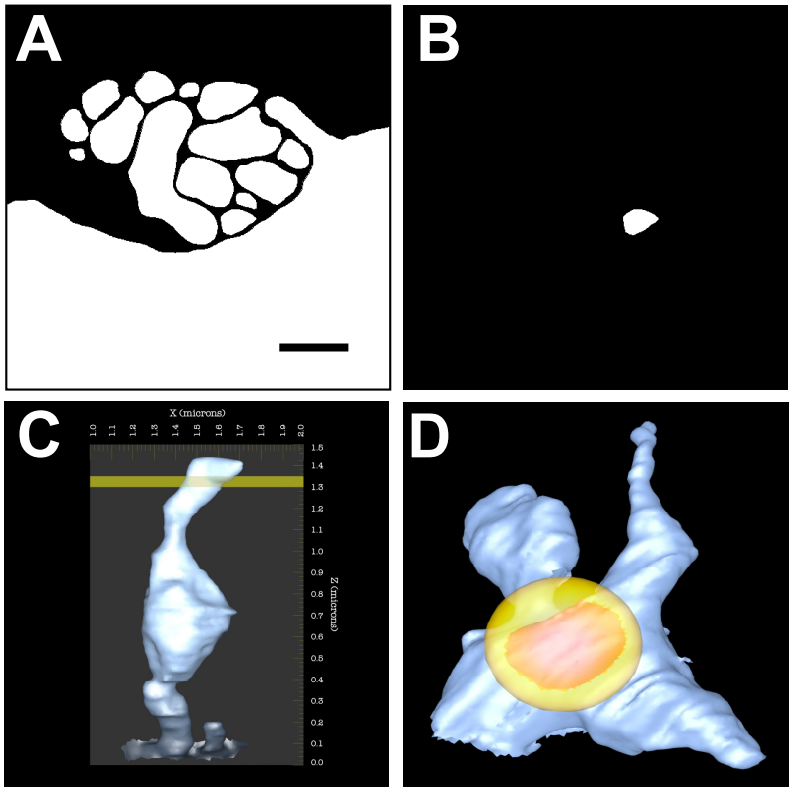

Figure S1

A Reaction Mechanisms for nAChRs:

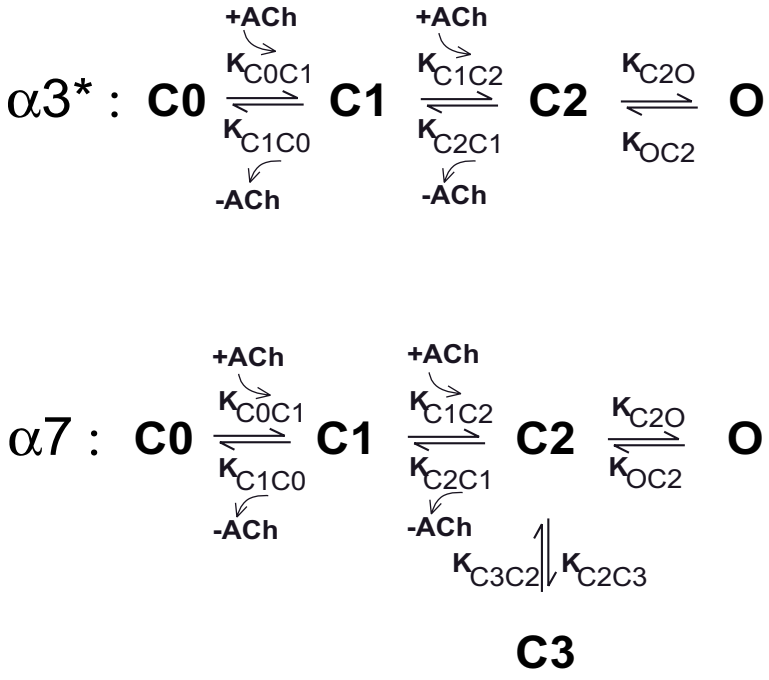

Rate Constants:

	α3*	α7
K_{C0C1} (K_+)	2(2.3 x10^6) $M^{-1}s^{-1}$ (*24*)	2(4.1 x 10^7 $M^{-1}s^{-1}$) (*25*)
K_{C1C0} (K_-)	84/s (*26*)	82.2/s (*10*)
K_{C1C2} (K_+)	2.3 x10^6 $M^{-1}s^{-1}$ (*24*)	4.1 x 10^7 $M^{-1}s^{-1}$ (*25*)
K_{C2C1} (K_-)	2(84)/s (*26*)	2(82.2) /s (*10*)
K_{C2O} (β)	513/s (*8*)	86.2/s (*10*)
K_{OC2} (α)	1000/s (*8*)	7641/s (*10*)
K_{C2C3} (K_{des})	N/A	879/s (*27*)
K_{C3C2} (K_{res})	N/A	26/s (*27*)

B Distribution Densities:

	PSD (μm^{-2})	Somatic non-PSD (μm^{-2})	Spine non-PSD (μm^{-2})
α7	N/A	N/A	3600 (*16*)
α3*	3600 (*18*)	80 (*18*)	80 (*18*)

Figure S2

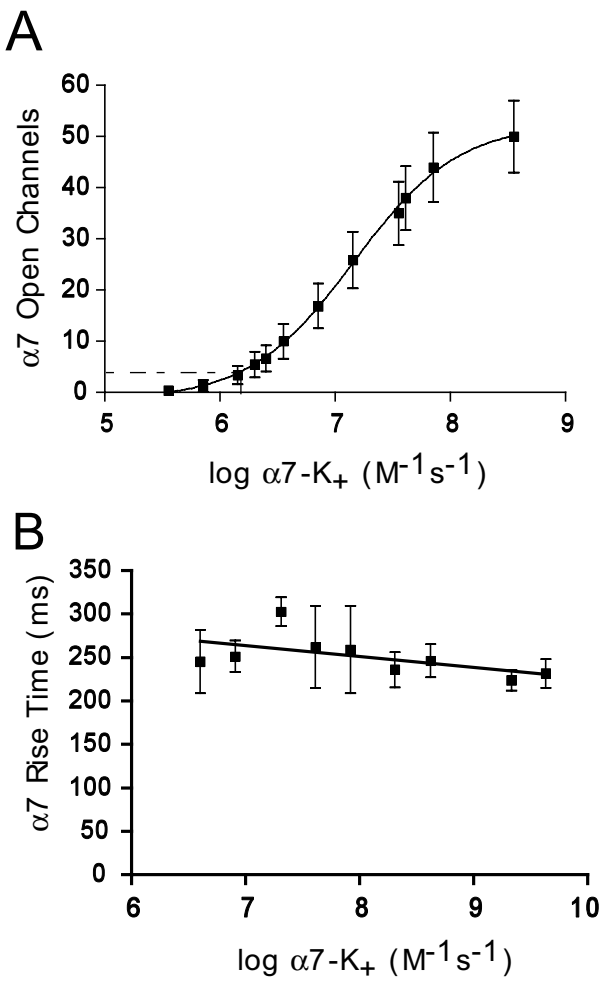
A
α7 Open Channels
60
50
40
30
20
10
0
5
6
7
8
9
log α7-K+ (M-1s-1)
B
α7 Rise Time (ms)
350
300
250
200
150
100
50
0
6
7
8
9
10
log α7-K+ (M-1s-1)

Figure S3